Ionic Conductivity, Structural Deformation, and Programmable Anisotropy of DNA Origami in Electric Field

Chen-Yu Li,[†] Elisa A. Hemmig,[‡] Jinglin Kong,[‡] Jejoong Yoo,[§] Silvia Hernández-Ainsa,[‡] Ulrich F. Keyser,[*,‡] and Aleksei Aksimentiev[*,⊥]

[†]Center for Biophysics and Computational Biology, University of Illinois at Urbana—Champaign, Urbana, Illinois 61801, United States, [‡]Cavendish Laboratory, University of Cambridge, Cambridge CB3 0HE, U.K., [§]Center for the Physics of Living Cells, University of Illinois at Urbana—Champaign, Urbana, Illinois 61801, United States, and [⊥]Department of Physics, University of Illinois at Urbana—Champaign, Urbana, Illinois 61801, United States

ABSTRACT The DNA origami technique can enable functionalization of inorganic structures for single-molecule electric current recordings. Experiments have shown that several layers of DNA molecules, a DNA origami plate, placed on top of a solid-state nanopore is permeable to ions. Here, we report a comprehensive characterization of the ionic conductivity of DNA origami plates by means of all-atom molecular dynamics (MD) simulations and nanocapillary electric current recordings. Using the MD method, we characterize the ionic conductivity of several origami constructs, revealing the local distribution of ions, the distribution of the electrostatic potential and contribution of different molecular species to the current. The simulations determine the dependence of the ionic conductivity on the applied voltage, the number of DNA layers, the nucleotide content and the lattice type of the plates. We demonstrate that increasing the concentration of Mg^{2+} ions makes the origami plates more compact, reducing their conductivity. The conductance of a DNA origami plate on top of a solid-state nanopore is determined by the two competing effects: bending of the DNA origami plate that reduces the current and separation of the DNA origami layers that increases the current. The latter is produced by the electro-osmotic flow and is reversible at the time scale of a hundred nanoseconds. The conductance of a DNA origami object is found to depend on its orientation, reaching maximum when the electric field aligns with the direction of the DNA helices. Our work demonstrates feasibility of programming the electrical properties of a self-assembled nanoscale object using DNA.

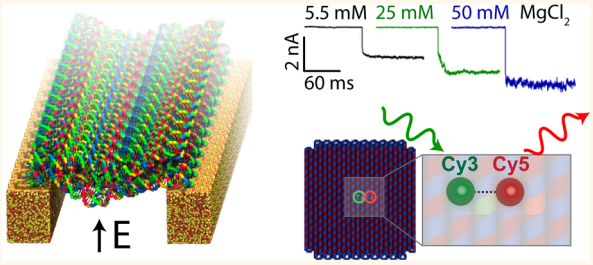

KEYWORDS: DNA nanotechnology · nanopore · molecular dynamics · FRET · DNA sequencing · anisotropic conductivity · self-assembly

Nanopores have emerged as versatile tools for single-molecule manipulation and analysis.[1−4] In a typical measurement, a charged biomolecule, DNA or a protein, is transported through a narrow pore in an insulating membrane by external electric field. The presence and, in some cases, the chemical structure of a biomolecule can be detected by measuring the change in the ionic current that flows through the nanopore.[5−15]

An accurate and reproducible process of nanopore fabrication is a necessary prerequisite for practical applications of the nanopore method. Differentiation between similar biomolecules may also require incorporation of specific ligands within the nanopores.[16,17] While more straightforward in the case of biological nanopores,[18] the attachment of specific binding sites with control over their position by chemical modification of nanopores in solid-state membranes continues to present considerable challenges.[19,20]

Combining biological materials with inorganic nanopores can give the resulting hybrid structure a more predictable shape and offer a route to biofunctionalization.[17,21−24] One such material is DNA origami, an object obtained by folding a long strand of DNA into a predefined pattern.[25] Since the DNA origami technique

* Address correspondence to ufk20@cam.ac.uk, aksiment@illinois.edu.

Received for review October 13, 2014 and accepted January 26, 2015.

Published online January 26, 2015
10.1021/nn505825z

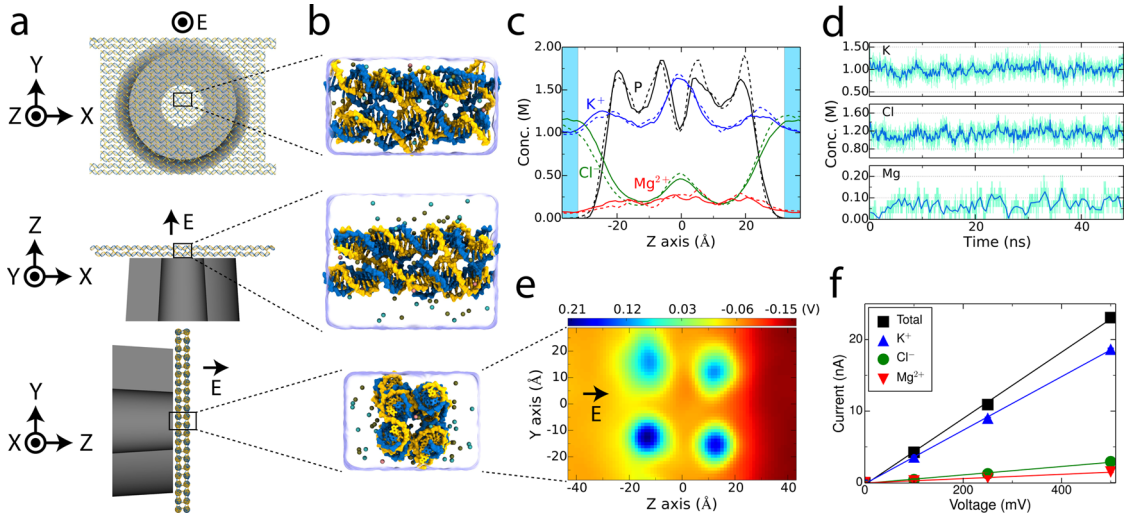

Figure 1. MD simulations of DNA origami conductivity. (a) Schematic of experimental setup. A DNA origami plate (yellow and blue) is placed on top of a nanocapillary (gray). (b) All-atom model of the experimental system. The scaffold and staple strands are shown in blue and yellow, respectively. Water is shown as a semitransparent molecular surface, Mg^{2+}, K^{+} and Cl^{-} ions are shown as pink, ochre and cyan spheres, respectively. For clarity, only 10% of the ions are explicitly shown. Under periodic boundary conditions, the DNA origami plate is effectively infinite in the *x*−*y* plane. (c) Distribution of ions across a DNA origami plate as a function of the distance from the plate's center. The distributions obtained from a 48 ns unrestrained equilibration simulation (solid lines) and a 48 ns simulation under a 100 mV applied potential (dashed lines) are plotted. Black lines indicate the distribution of DNA phosphorus atoms. The concentration profiles were computed by averaging over the *x*−*y* plane and the simulation trajectories using 1 Å bins. Blue areas indicate the parts of the system where the bulk ion concentration was computed. (d) Bulk concentration of K^{+}, Cl^{-} and Mg^{2+} ions *versus* simulation time under a 100 mV applied potential. (e) Simulated distribution of the electrostatic potential at a 100 mV applied potential. The map was obtained by averaging the instantaneous distributions of the electrostatic potential over the 48 ns MD trajectory and the *x* axis. (f) Ionic current *versus* applied potential. Each data point was obtained from a 48 ns trajectory. All data presented in this figure are for a two-layer square-lattice DNA origami plate at 50 mM Mg^{2+} /1 M KCl bulk ion concentration.

was first demonstrated in 2006, it has been used to assemble a variety of complex three-dimensional objects.[26−31] A number of auxiliary components, such as fluorescent labels, nanoparticles or enzymes, can be incorporated into the origami objects with base-pair accuracy.[32−41] The nanometer precision of the DNA self-assembly process and compatibility with typical conditions of nanopore experiments make DNA origami an attractive candidate for the construction of hybrid nanopores.[42−44]

Hybrid nanopore systems based on DNA origami have already been characterized experimentally.[45−53] A cone-like DNA origami funnel was inserted into a silicon nitride nanopore and used for the detection of λ-DNA.[45] Plate-like DNA origami objects were placed on top of nanopores in solid-state membranes and used for the detection of proteins and double-stranded DNA (dsDNA).[46] Adding single-stranded DNA (ssDNA) overhangs to the DNA origami structure was shown to facilitate the detection of ssDNA translocation.[46−48] DNA origami plates were also combined with glass nanocapillaries and used for single-molecule detection.[48,52] In general, the conductance of the hybrid pores was found to depend on the structure of the DNA origami component,[53] the ionic concentration of the solution[53] and the magnitude of the electric field.[52,53] The latter effect was presumably caused by the deformation of the DNA origami structure. DNA origami has also been combined with lipid bilayer membranes.[47,49,50] Functionalized with cholesterol, a DNA origami channel was inserted into a lipid bilayer and used to detect and distinguish ssDNA.[47] Simpler designs employed partial neutralization of the DNA backbone[49] or attachment of two porphyrin moieties.[50]

In this study, we use all-atom molecular dynamics (MD) simulations to characterize the ionic conductivity and deformability of DNA origami plates. Complementing previous experimental work, we investigate the effects of the DNA origami structure, electrolyte conditions and the strength and direction of the electric field. Our simulations provide a complete atomic-level account of the ion transport process, detailing previously unknown effects of the DNA origami sequence, magnesium ion concentration and the electro-osmotic flow. Experiments based on electric current recordings and Förster resonance energy transfer (FRET) confirm the predictions of the MD simulations. We demonstrate feasibility of controlling the electrical conductivity of a DNA self-assembled object by its nucleotide sequence, an ability that may find applications in nanofluidic electronics.

RESULTS AND DISCUSSION

MD Simulations of Ionic Conductivity of a DNA Origami Plate. Figure 1a schematically illustrates a system for the experimental characterization of the ionic conductivity of DNA origami plates.[52] This particular image

features a two-layer square-lattice DNA origami that measures approximately 57.8 nm (170 bp) × 52.8 nm (24 helices) × 4.4 nm (2 helices). Although it is technically possible to simulate this entire DNA origami object using a fully atomistic model, such simulations are computationally expensive and are not even necessary because the full-length plate is a repetition of a unit cell pattern. Thus, the majority of our MD simulations were performed on all-atom models of the unit cell, such as the one shown in Figure 1b. The initial coordinates of the models were obtained by converting the caDNAno designs[54] to the atomistic representation following a previously described protocol.[55] By introducing covalent bonds across the periodic boundaries, the DNA origami plates were made effectively infinite in the $x-y$ plane. The plates were immersed in ionic solution, minimized and equilibrated as described in Materials and Methods.

Figure 1c illustrates a typical distribution of ions in a fully equilibrated system. At the scale of the simulation system, the distribution is nonuniform. Within the volume occupied by DNA origami, the concentration of cations is enhanced and the concentration of anions is reduced, in accordance with the results of our previous studies.[56,57] In a distance of approximately 20 Å from the DNA origami plate, ion concentration profiles flatten out. We used a rectangular volume away from the DNA (blue area in Figure 1c) to determine the "bulk" concentrations of ions. As the equilibrium distribution of ions is highly nonlinear, it was not possible to determine *a priori* the number of K^+, Cl^- and Mg^{2+} ions that were needed to produce a desired bulk concentration. Hence, several iterative equilibration runs (~50 ns each) were required to bring the bulk ion concentration to the target value.

To produce ionic current, a uniform electric field, E, was applied normal to the DNA origami plate, inducing an electric potential difference, $V = -EL$, where L was the length of the simulation system in the direction of the applied field.[58] The application of the electric field had a minor effect on the distribution of ions within the DNA origami plate, Figure 1c. The bulk ion concentration remained stationary, Figure 1d. Figure 1e shows a typical distribution of the electrostatic potential in the simulation system corresponding to a 100 mV voltage difference across the DNA origami plate. The distribution is highly nonlinear within the plate. The approximate location of the DNA helices can be discerned as regions of elevated electrostatic potential, which is produced by the partial positive charge on the DNA bases; the negative charge of the DNA backbone is effectively screened by the counterions. The current of ions produced by the electric field can be readily determined by summing up ion displacements over the simulation system and the MD trajectory.[58] The ionic current appears to increase linearly with voltage and be carried predominantly (80−85%) by potassium ions, Figure 1f. Animation S1 (Supporting Information) illustrates the process of ion permeation through the DNA origami plate.

Effect of Number of Layers, Lattice Type, and Nucleotide Composition. To examine how the ionic conductivity of a DNA origami plate depends on the number of DNA layers, we built and equilibrated square-lattice DNA origami systems containing two (SQ2), four (SQ4), and six (SQ6) DNA layers, Figure 2a; the bulk concentrations of Mg^{2+} and KCl were ~250 mM and 1 M, respectively. The equilibrated structures were simulated under applied bias of 100, 250, and 500 mV for 48 ns each. At the same bias, systems having a larger number of layers showed a lower ionic current, Figure 2b. The dependence of the current on the number of layers is, however, nonlinear: the SQ2 system appears to be more permeable to ions than the SQ4 system at doubled applied bias.

Knowing the dimensions of the simulation system (L_x, L_y and L_z) and the extension of the DNA origami along the direction of the applied field L_o, the conductivity of the DNA origami plate $\sigma_{o,z}$ can be computed from a simple circuit model as

$$\sigma_{o,z} = \frac{\langle L_o \rangle \langle I_z \rangle}{V L_x L_y - \rho_s \langle I_z \rangle (L_z - \langle L_o \rangle)} \quad (1)$$

where V is the applied potential, I_z is the average current normal to the plate and ρ_s is the resistivity of the solution. Figure S1 and Supporting Information Methods provide a detailed description of the circuit model.

Figure 2c shows the conductivity of the SQ2, SQ4 and SQ6 plates as a function of applied potential. The conductivity of the four- and six-layer structures is approximately the same and does not depend on the applied bias. The conductivity of the SQ2 is higher and increases with the applied potential. Given that the solution resistivity (Figure S2) and the cross-sectional area of the SQ2, SQ4 and SQ6 systems (Figure S7b) are approximately the same, the apparent difference in the conductivity is caused by the differential extension of the DNA origami along the direction of the applied field. Indeed, the thickness per layer of the SQ2 plate is ~12% larger than that of the SQ4 and SQ6 systems and increases with the applied potential, Figure S7c. The fraction of the plate's volume occupied by DNA is lower in the two layers of the SQ2 plate than in any two layers of the SQ4 or SQ6 structures, and hence the SQ2 structure has a higher conductivity. The more compact structure of the four- and six-layer plates is a consequence of their design. The unit cell of the two-layer plate contains only two Holliday junctions between the two layers, which is considerably less dense than six and ten interlayer junctions in the four- and six-layer plates, respectively, Figures S3−S5. Furthermore, staple strands in the SQ4 and SQ6 plates can bridge up to three consecutive layers.

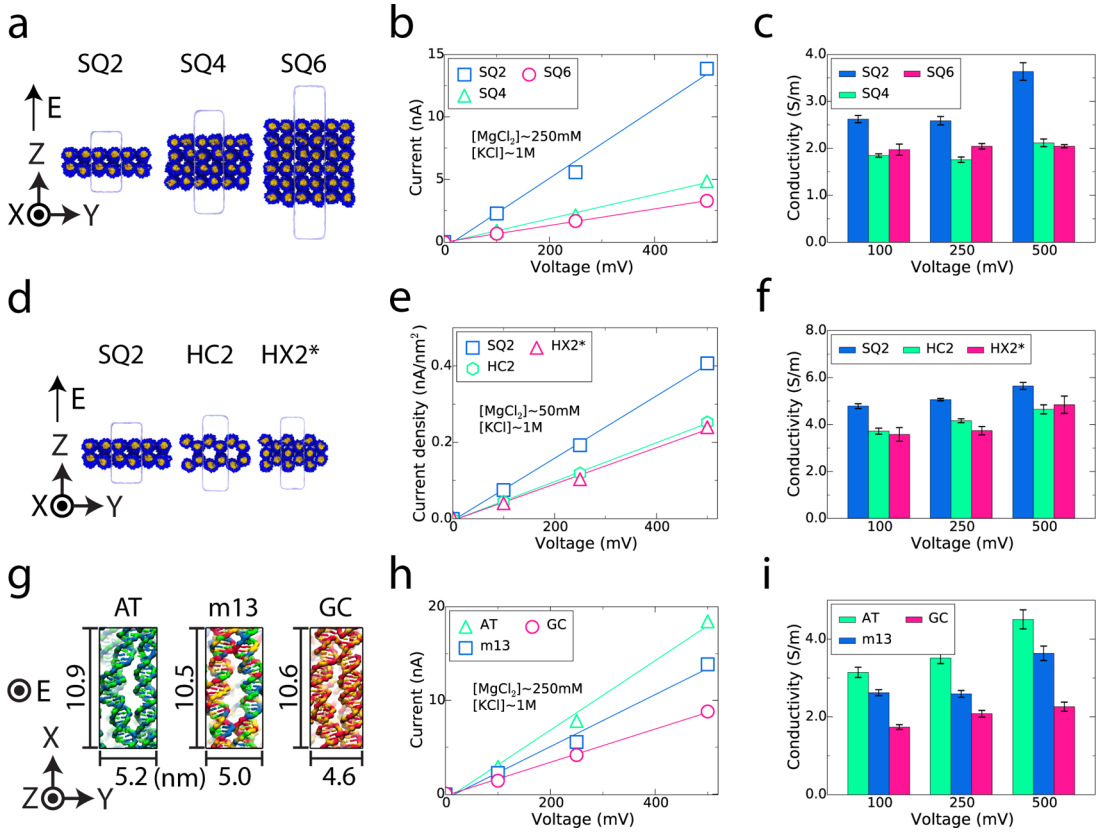

Figure 2. Ionic conductivity of DNA origami plates. (a) Simulation systems containing two-, four- or six-layer DNA origami plates. The backbone of DNA is shown in blue, the DNA bases are shown in yellow. The unit cell of each simulated system is shown as a semitransparent surface. (b) Current−voltage dependence of the two-, four- and six-layer DNA origami plates. Each data point was obtained from a 48 ns trajectory. (c) Electrical conductivity of square-lattice DNA origami *versus* the number of DNA layers. Data in panels b and c correspond to ~250 mM Mg^{2+} /1 M KCl bulk ion concentration. (d) Simulation systems containing units cells of the square-lattice, honeycomb and hexagonal DNA origami plates. (e) Ionic current density *versus* lattice type. (f) Ionic conductivity *versus* lattice type. Data in panels e and f correspond to ~50 mM Mg^{2+} /1 M KCl bulk ion concentration. (g) Representative conformations of a square-lattice DNA origami plate containing 100% adenine−thymine (AT), 100% cytosine−guanine (CG) or a 45/55% AT/CG mixture (m13) of DNA base pairs. A, T, C and G nucleotides are shown in blue, green, red and yellow, respectively. The average dimensions of the equilibrated structures are indicated in the images. (h,i) Ionic current (h) and ionic conductivity (i) *versus* applied voltage for the three systems shown in panel g. The AT and CG systems contained the same number of magnesium ions; the number of Mg^{2+} ions in the m13 system was 2.5% higher than in either AT or CG system. Because of the differential affinity of Mg^{2+} ions to AT and CG base pairs the equilibrium concentrations of Mg^{2+} were 243.6 ± 2.2 (AT), 249.4 ± 2.2 (m13) and 209.4 ± 2.1 (CG) mM. Data in panels b, e and h were obtained from 48 ns trajectories; the lines indicate the linear fits to the data. Error bars in panels c, f, and i show the standard error computed over five ~10 ns fragments of the 48 ns trajectory.

In order to determine how the lattice type can affect ion permeation through DNA origami plates, we constructed two additional systems based on the honeycomb (HC2)[26] and hexagonal (HX2*)[31] lattices, Figure 2d. Here, we use an asterisk to distinguish the simulated hexagonal lattice system from the one realized in experiment.[31] We built our HX2* system by inserting a DNA double helix into the central cavity of a honeycomb lattice. In contrast to the system realized in experiments, the central double helix was not connected to the surrounding DNA helices through Holliday junctions. To compare the ion permeability of different DNA structures, we plot in Figure 2e the ionic current per unit area (the unit cells of the SQ2 and HC2 structures have different areas). Overall, the current density of the SQ2 plate was roughly twice as high as for the HC2 and HX2* plates at the same applied bias whereas the current densities of the HC2 and HX2* plates were comparable. Taking into account the dimensions of the plates in the direction of the applied field, the conductivity of the SQ2 plate is estimated to be about 120−130% of the conductivity of the HC2 plate, Figure 2f. The higher conductivity of the SQ2 plate primarily results from the lower density of the DNA nucleotide per unit area of the plate, Figure S8b, and a higher nearest-neighbor inter-DNA (NNiD) distance, Figure S8d. One would intuitively expect the conductivity of HX2* to be lower than that of HC2, given its more compact structure. However, our data shows that the difference in conductivity between HC2 and HX2* is not significant. As the central helix in our HX2* was not connected to the surrounding helices, the electrostatic repulsion between the central helix and the surrounding helices made the entire structure

more diffuse in comparison to the HC2 structure. Thus, the NNiD distance is higher for the HX2* structure than for HC2, Figure S8c,d. The larger NNiD distance of the HX2* structure compensates for the higher (than HC2) nucleotide density of HX2*, Figure S8.

Our simulations suggest that the conductivity of a DNA origami plate can also depend on its nucleotide content. Figure 2g shows typical conformations of three SQ2 plates that differ from one another in their design only by their nucleotide content. The nucleotide content appears to affect the average distance between DNA helices within the plate as well as the distance between Holliday junctions along the helices, with the AT plate being most sparse and the CG plate most compact. Animations S2–S4 illustrate conformational dynamics of the three plates. The simulated ionic current, Figure 2h, and the ionic conductivity, Figure 2i, depend on the nucleotide content, with the AT plate being the most leaky and the CG plate being the most ion tight. The current and conductivity of the plate made from a fragment of the m13mp18 genome (AT content of 45%) fall in between the data obtained for the AT and CG plates. The sequence dependence can be rationalized taking into account the differential affinity of Mg^{2+} toward AT and CG DNA pairs.[57,59] The CG-rich DNA origami was found to have a higher concentration of Mg^{2+} inside the origami, Figure S9a,b. The higher concentration of Mg^{2+} reduced the electrostatic repulsion between the DNA helices in the origami, resulting in more compact structures, Figure S9c,d. The higher degree of expansion of the AT system makes it more permeable to ions in comparison to the GC system; the properties of the m13 system fall in between of the AT- and CG-rich systems.

Magnesium Affects the Structure and Conductivity of DNA Origami Plates. The results of our MD simulations suggest that the ionic current through the same DNA construct (SQ2) under the same applied voltage drops by ~43% when the bulk concentration of Mg^{2+} increases from 50 to 250 mM (Figure 1f and Figure 2b). Using an experimental setup shown in Figure 3a, we systematically examined the dependence of the DNA origami conductivity on Mg^{2+} concentration. Table S3 and Figure S10 detail design and characterization of the plates used for these experiments. The DNA origami plates were repeatedly trapped onto the nanocapillary; the trapping events were discerned by the drop of the ionic current, Figure 3a. The magnitude of the ionic current drop increased as the concentration of Mg^{2+} increased, consistent with the behavior observed in our MD simulations of the origami plates.

Repeating the trapping experiments at four different magnesium concentrations (5.5, 25, 50, and 100 mM $MgCl_2$) while keeping the concentration of KCl at 1 M, we measured the relative change of hybrid nanocapillary-DNA origami conductance. To directly compare the results of the trapping experiments using

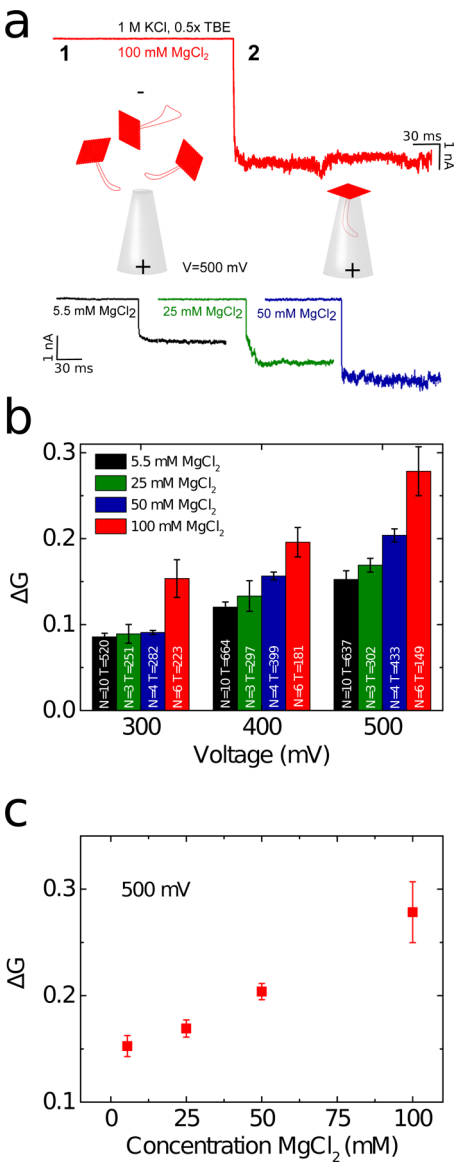

Figure 3. Experimental characterization of DNA origami conductivity. (a) Schematic representation of a hybrid DNA origami–quartz nanocapillary structure along with typical ionic current signatures measured at 500 mV and in 1 M KCl, 0.5× TBE (Tris/Borate/EDTA, Table S6), pH ≈ 8.3. (Top) Baseline current I_0 corresponds to ionic flow through the bare nanocapillary (part 1 of the trace). Once the DNA origami plate is trapped, the reduced ionic current level I_{hybrid} indicates the successful formation of a hybrid structure (part 2 of the trace). (Bottom) Representative examples of hybrid structure formation signatures for $MgCl_2$ concentrations of 5.5 (black), 25 (green) and 50 (blue) mM, all at 500 mV. Larger current reductions were observed at higher $MgCl_2$ concentrations. A representative trace at 100 mM $MgCl_2$ is shown in the top panel. (b) The relative conductance change $\Delta G = 1 - G_{hybrid}/G_0$ *versus* $MgCl_2$ concentration and applied potential. G_{hybrid}/G_0 is calculated from the ratio of the ionic current levels (2) and (1), I_{hybrid}/I_0. (*N*) denotes the number of experiments or nanocapillaries used and (*T*) the total number of repeated trappings to measure the averaged ΔG at 5.5 (black), 25 (green), 50 (blue) and 100 (red) mM $MgCl_2$ for three different applied potentials (300, 400, and 500 mV). (c) ΔG *versus* $MgCl_2$ concentration at a 500 mV applied potential. Error bars correspond to the standard error of the mean of ΔG.

capillaries of different diameters, we define the relative conductance change $\Delta G = 1 - G_{hybrid}/G_0$, where G_{hybrid}/G_0 is the ratio between the conductance of the bare nanocapillary G_0 and the conductance of the hybrid DNA origami−nanocapillary structure G_{hybrid} upon trapping. G_{hybrid}/G_0 can be directly inferred from measuring the ratio I_{hybrid}/I_0 between the corresponding ionic current levels I_{hybrid} and I_0, Figure 3a. For each magnesium concentration, we tested a range of nanocapillaries (denoted by number of experiments N in Figure 3b) and performed several hundred trappings (denoted by total number of trappings T in Figure 3b) at applied potentials of 300, 400, and 500 mV, respectively.

From our measurements we can conclude that there is both a voltage and $MgCl_2$ dependence of ΔG. At each $MgCl_2$ concentration, a higher voltage leads to a higher ΔG, Figure 3b; the voltage dependence is more pronounced for higher $MgCl_2$ concentrations. The voltage dependence suggests that the voltage applied to trap the DNA origami structures leads to deformations as expected from our earlier measurements.[52] Figure 3c shows ΔG at 500 mV as a function of the $MgCl_2$ concentration. We observe that ΔG increases monotonically as $[Mg^{2+}]$ of the solution is increased. We note that the increase in the $MgCl_2$ concentration from 5.5 to 100 mM only leads to a 12.4% increase in the conductivity of the bulk solution from 10.5 to 11.8 S/m. However, ΔG is enhanced by a factor of 2 from ~0.15 to ~0.30 at 500 mV, Figure 3c. This further highlights the strong interaction between the Mg^{2+} ions and the DNA origami plate.

MD simulations elucidated the microscopic origin of the $[Mg^{2+}]$ dependence of the plate's conductivity. Figure 4a shows the area of the SQ2 plate simulated at three different values of $[Mg^{2+}]$ and 1 M KCl. Although the area undergoes considerable fluctuations at a time scale of hundreds of nanoseconds, the average value decreases as $[Mg^{2+}]$ increases. Figure 4b shows the representative conformations of the three systems featured in Figure 4 a; the dimensions of the unit cell are highlighted. Animations S4, S5, and S6 illustrate these simulation trajectories. Temporal fluctuations of the area were seen to become less pronounced as $[Mg^{2+}]$ was increased, Figure S11. Figure 4c shows the simulated dependence of the area on $[Mg^{2+}]$ in the 0 to 250 mM range. For each data point, the corresponding system was simulated for more than 490 ns, Table S1; the average area and $[Mg^{2+}]$ concentration were determined by averaging over the last 400 ns of each MD trajectory. The plot reveals a linear correlation between $[Mg^{2+}]$ and the area of the DNA origami plate. By setting the area of each simulation system to its average value and applying an external field, the simulations determined the dependence of the plate's conductivity on the magnesium concentration: the conductivity linearly decreases as $[Mg^{2+}]$ increases, Figure 4c, in agreement with the experimental observations. Thus, increasing the concentration of Mg^{2+} ions makes the DNA origami plate more compact, decreasing its conductivity.

To independently verify the compaction of the DNA origami plates induced by Mg^{2+}, we performed FRET measurements on DNA origami labeled with Cy3 (donor) and Cy5 (acceptor) dyes. The fluorophore attachment sites were located in the center of the DNA origami plate and within the same plane of the plate. We prepared three variants of the structure having the Cy3−Cy5 pair aligned parallel, perpendicular and diagonal to the direction of the DNA helices, Figure 4d. The structural integrity of the fluorescently labeled plates was confirmed by agarose (1%) gel electrophoresis, Figure S12. For each arrangement of the Cy3−Cy5 pair, FRET measurements were performed by gradually increasing the concentration of $MgCl_2$ in the same cuvette and collecting the emission spectra at $MgCl_2$ concentrations of 5.5, 55.5, 105.5, and 205.5 mM. This allowed us to avoid possible artifacts associated with sample variation. The apparent FRET efficiency E^* was determined using a ratiometric approach, $E^* = I_A/(I_D + I_A)$, where I_A and I_D were the emission intensities of the acceptor and donor dyes, respectively, upon donor excitation. The intensities I_D and I_A were obtained by calculating the area under the emission spectra corresponding to the donor and acceptor signals, Figure S13. The apparent FRET efficiency was found to depend both on the orientation of the Cy3−Cy5 dyes and $MgCl_2$ concentration, Figure 4e. For the perpendicular orientation, we observed a clear increase in E^* by ~20% as the $MgCl_2$ concentration increased from 5.5 to 205.5 mM, which we interpret as reduction of the distance between the labels. A similar trend was observed for the diagonal orientation of the dyes. For labels placed along the DNA helix, increasing the $MgCl_2$ concentration from 5.5 to 205.5 mM leads to a decrease in E^* by ~15%.

For comparison, we plot in Figure 4f the estimated distance between the dye attachment sites measured from MD trajectories of the SQ2 system. In the experiment, the dye labels were attached near scaffold crossovers of the origami plates. Our minimal models of the plates contained neither the dye molecules nor crossovers of the scaffold strand. Hence we used the distance between phosphorus atoms to estimate the distance between the dyes. For the parallel and diagonal arrangements of the Cy3−Cy5 pair, we computed the average distance between all pairs of phosphorus atoms that satisfied the distance restraints of the experimental design, Figure 4d. For the perpendicular arrangement, we used the average dimension of the simulation system along the y axis. The distances were averaged over the 400 ns fragments of the respective trajectories sampled every 2.4 ps. A higher separation

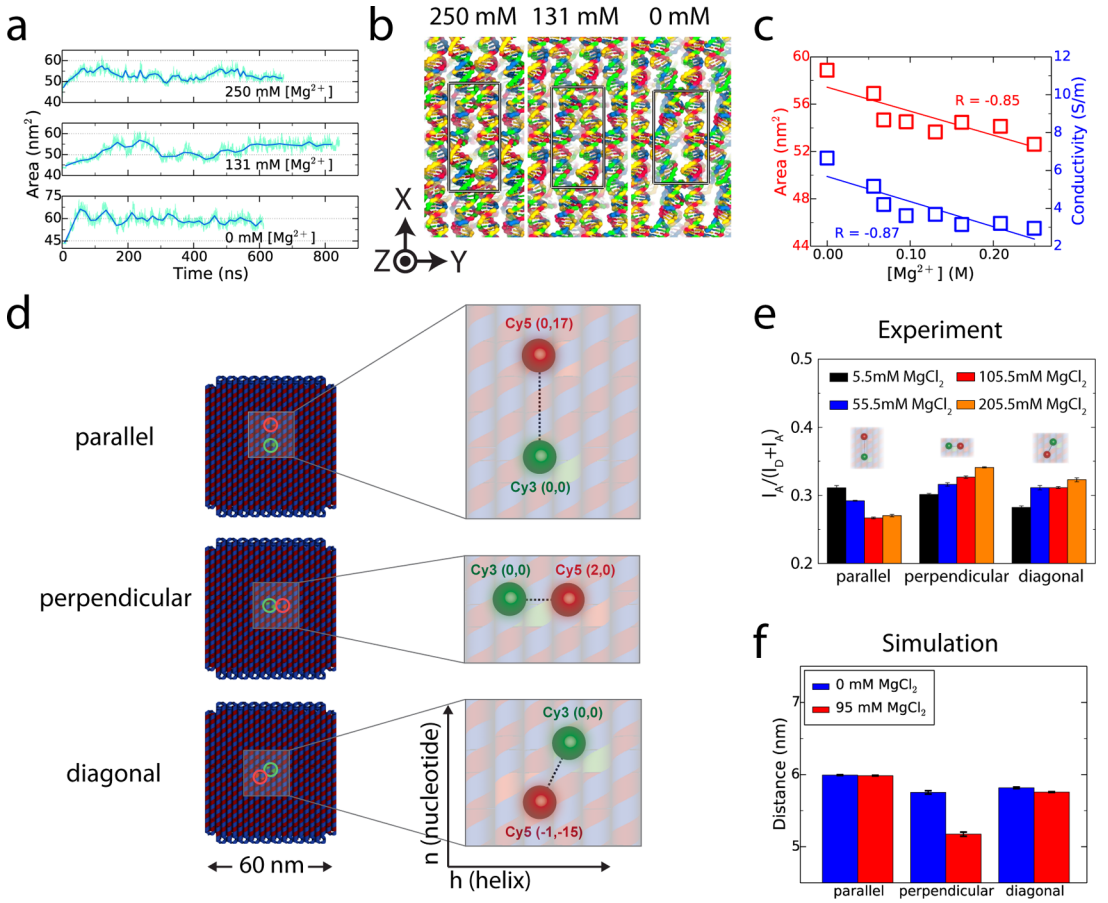

Figure 4. Mg^{2+} concentration regulates ionic conductivity by altering the area of DNA origami. (a) Cross-sectional area of an SQ2 plate *versus* simulation time for several values of bulk Mg^{2+} concentration. The area is computed within a plane normal to the direction of the ionic current ($x-y$ plane, Figure 1). (b) Representative conformations of an SQ2 plate at several values of bulk Mg^{2+} concentration. A rectangle indicates the unit cell of the corresponding simulation system. The areas of the unit cells pictured are 53 (250 mM), 54 (131 mM) and 59 (0 mM) nm^2. (c) Simulated dependence of the SQ2 plate area (left) and ionic conductivity (right) on bulk concentration of Mg^{2+}. Lines are linear fits to the data. For each fit, the Pearson's correlation coefficient R is indicated in the plot. (d) Design of DNA origami plates for FRET measurements of Mg^{2+}-dependent compaction. Two fluorescently labeled staples formed a FRET pair at the center of each plate. The Cy3 donor dye (green) and the Cy5 acceptor dye (red) were aligned parallel, perpendicular and diagonal with respect to the DNA helix direction of the origami. The circles mark the location of the modified staples within the DNA origami plate. Insets specify the location of the Cy3−Cy5 pairs for each of the three designs. The DNA origami coordinates (h, n) denote the helix (h) and nucleotide (n) number relative to the Cy3 dye attached at the origin (0, 0). (e) FRET efficiency E^* at a background concentration of 1 M KCl, 0.5× TBE and $MgCl_2$ concentrations of 5.5 (black), 55.5 (blue), 105.5 (red), 205.5 (orange) mM for the parallel, perpendicular and diagonal placement of the FRET pair. (f) The average distance between the estimated locations of the donor and acceptor dyes in MD simulations of the SQ2 plate at two Mg^{2+} concentrations.

between the dyes was observed at lower concentrations of Mg^{2+} for the perpendicular arrangement of the FRET pair, in qualitative agreement with the experiment. No statistically significant change in the FRET pair separation was determined for the parallel and diagonal arrangements of the labels.

Deformation of DNA Origami Plates by Electric Field. Being negatively charged, a DNA origami plate moves in an external electric field, loading itself on top of a nanocapillary or a solid-state nanopore.[45,46,48,52] Once placed on a solid-state support, the motion of the plate is arrested; however, further deformation of the internal structure can occur under the action of the electric field.

To evaluate the nature and extent of the structural deformation, we first examined the behavior of the origami plates in MD simulations carried out without the support structure. In those simulations, a harmonic potential was applied to the center of mass of the DNA origami plate to limit the drift of the plate in the external field. Figure 5 summarizes the results of our analysis. In all two-layer DNA origami structures, the distance between the layers was observed to increase with the magnitude of the electric field, Figure 5a,b and Animations S7−S9. We suggest that the larger deformations observed in the HX2* structure as compared to the HC2 structure were due to the missing Holliday junctions in our design, Figure 5b. Such deformations were reversible. For example, by switching the electric field on and off, the distance between the layers of the SQ2 structure could be increased and reduced at a hundred nanosecond time scale, Figure 5c and

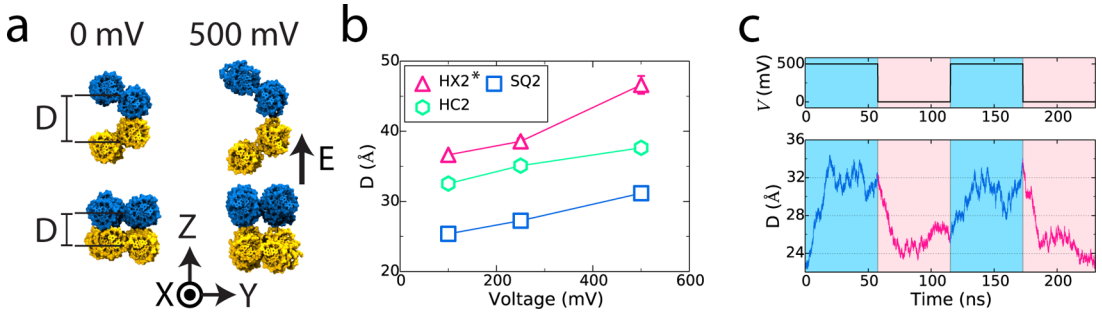

Figure 5. Modulation of the DNA origami structure by applied voltage. (a) Representative conformations of the SQ2 and HC2 DNA origami plates in the presence and absence of an external electric field (bias = 500 mV). D defines the distance between the centers of mass of the scaffold strand in the upper and bottom layers of the DNA origami plate. (b) The distance between the layers of the DNA origami plates *versus* applied voltage. Lines are guides to the eyes. Data obtained at ~50 M Mg^{2+}/1 M KCl bulk ion concentration. (c) Reversible swelling and shrinking of the DNA origami plate by applied voltage. Animation S7 illustrates this MD trajectory. This set of simulations was performed at ~250 mM Mg^{2+}/1 M KCl bulk ion concentration.

Animation S7. Analysis of the MD trajectories revealed the hydrodynamic drag of the electro-osmotic flow[60] to cause such deformation of the DNA origami plates (see below).

A different mode of deformation was observed when a DNA origami plate was put on top of a solid support, Figure 6a, which is a typical situation realized in experiment. For this set of MD simulations, we built a ~15 nm nanogap structure from amorphous SiO_2 and placed a fragment of SQ2 structure 1 nm away from the SiO_2 structure, leaving space for the addition of Mg^{2+}-hexahydrate. In contrast to our previous setup, the origami plate was only made effectively infinite in *y* direction and was double in length of the SQ2 plate, Figure S6. Following ~20 ns equilibration, the systems were subjected to applied potentials of different magnitudes.

Figure 6a displays the structures observed at the end of the MD runs. The plate is observed to deform and move into the gap as the magnitude of the applied bias increased, Animations S10–S12. To quantify the degree of such motion, we plot in Figure 6b the average distance from the origami plate's center of mass and the nearest surface of the SiO_2 structure, *H* (also see Figure S14). The plate moved in by several Å, on average. Coincident with bending, the layers of the DNA origami structure move apart, just like in our previous simulations of bare plate system, Figure 5. Under the same voltage, the layers in the bare and gap systems move apart by approximately the same degree, Figure 6b. Bending of the plate increases the density of DNA nucleotides, in comparison to the density of an equilibrated SQ2 plate, Figure 6c. At a 1 V bias, the DNA origami was observed to permeate through the nanogap structure, Animation S13.

The observed deformation of the plate structure in the hybrid system is caused by a delicate balance of the hydrodynamic drag that pushes the DNA origami away from the gap and the electrostatic force that pulls the origami into the gap. In Figure 6a, we characterize the nonuniform water flux pattern by indicating the direction (arrow) and magnitude (color and line width) of the local flux using a streamplot. Figure 6d compares the total flux of water through the bare and hybrid DNA origami structures. To enable direct comparison between the two systems, the figure shows the total water flux through the *x*–*y* plane divided by the *x*–*y* area of the system (bare origami) or the area of the gap (hybrid system). The flux is smaller in the case of the hybrid structure because of the presence of the SiO_2 structure.

Figure 6e compares the *I*–*V* curves of the hybrid and bare DNA origami structures normalized by the area. The *I*–*V* curves are slightly nonlinear in both cases: the current increases faster than linearly in the case of the bare origami structure and slower than linearly in the case of the hybrid structure. To make the nonlinear behavior more obvious, we plot in Figure 6f the relative conductance blockade ΔG that was previously introduced to describe the nanocapillary measurements. ΔG clearly decreases in the case of a bare structure and increases in the hybrid system.

The nonlinear behavior is explained by the deformation of the origami plates. The bare system becomes more sparse as the voltage increases, Figure 5, allowing more ions to pass. The hybrid system becomes more dense, additionally obstructing the passage of ions, Figure 6c. For comparison, ΔG measured experimentally using the nanocapillary setup is plotted *versus* voltage in Figure 6g. The simulated and experimental dependencies are in good qualitative agreement. Direct quantitative comparison, however, is not possible as the simulated and measured structures significantly differ from one another in terms of geometry: an infinite gap was considered in simulations, whereas a long conical capillary was used in experiment. Another factor is the presence of the guiding leash in the experiment, which could cause an additional deformation of the structure.[52]

Our simulations also provide an estimate of the leakage current between the DNA origami and the SiO_2 surface. Within 0.5 nm of the silica surface, the ionic

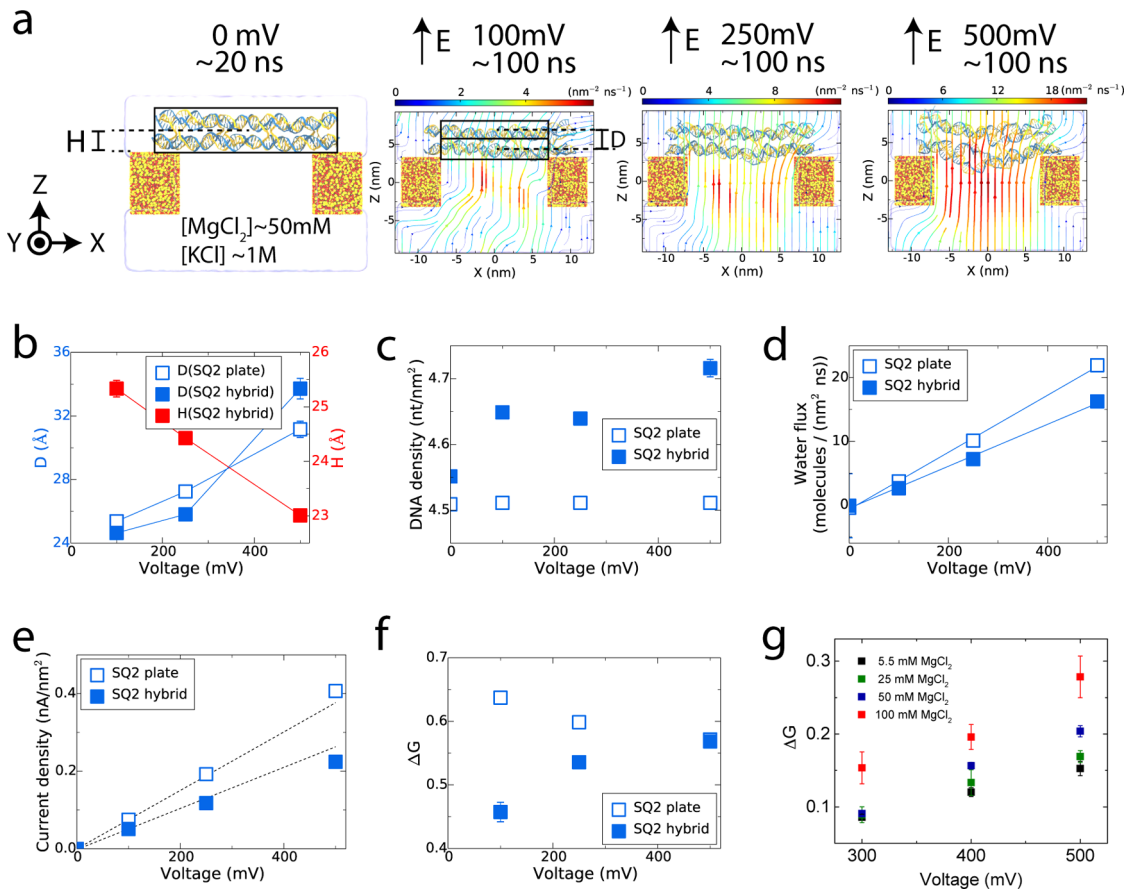

Figure 6. Electrical conductivity of a hybrid DNA origami/SiO_2 structure. (a) Representative conformations of a hybrid structure under applied voltage of different magnitudes. Each simulation system contained a two-layer square-lattice DNA origami, colored in blue (scaffold) and yellow (staples), placed on top of a SiO_2 nanogap, colored in yellow (Si) and red (O). Under periodic boundary conditions employed in the MD simulations, the SiO_2 structure is effectively infinite in the $x-y$ plane, whereas the DNA origami is effectively infinite only in the y direction. For the systems simulated under applied potential, the magnitude of the local water flux is indicated using a colormap where the arrow heads indicate the direction of the flux lines. See Supporting Information Methods for details of computation of the flux field and its visualization. All systems were simulated at ~50 mM Mg^{2+} /1 M KCl bulk ion concentration. (b) The distance between the center of mass of the SQ2 plate and the top surface of SiO_2 (right) and the distance between the upper and lower layers of the SQ2 plate (left) *versus* applied voltage (also see Figure S14). For the hybrid structure, only the part of the DNA origami directly on top of the gap in SiO_2 was considered for calculation of D. (c) Density of the DNA origami structure on top of the SiO_2 gap *versus* applied voltage. The density of the SQ2 plate is shown for comparison. (d) Water flux through the hybrid and bare plate structures *versus* voltage. (e) Current density *versus* applied voltage for the hybrid and plate structures. Dashed lines are drawn from the origin through the first (100 mV) point of each dependence to emphasize the nonlinear behavior. (f) Simulated dependence of the relative conductance change ΔG on applied voltage for the hybrid and plate structures. (g) Experimental dependence of ΔG on applied voltage at several Mg^{2+} concentrations.

current was found to amount to at most 6% of the total current for the structures considered.

Anisotropic Conductivity of DNA Origami Structures. To determine if the intrinsically anisotropic structure of a DNA origami object can cause it to have anisotropic electrical properties, we simulated the m13 SQ2 system applying the electric field parallel and perpendicular to the DNA helices, Figure 7a. Knowing the resulting ionic currents I_x and I_y, the ionic conductivity of the SQ2 plate parallel ($\sigma_{o,x}$) or perpendicular ($\sigma_{o,y}$) to the DNA helix direction can be computed using an electric circuit model that approximates the simulated system as resistors connected in parallel, Figure S1b,c. Figure 7b specifies the simulated directional conductivity of the plate. The DNA origami is predicted to be more conductive parallel to the DNA helices than perpendicular to them. The conductivity of the plate along the z direction, $\sigma_{o,z}$, which is plotted in Figure 2f, is similar to that of $\sigma_{o,y}$, but exhibits larger dependence on the voltage as the origami plate was free to expand in that direction.

To test the predictions of the MD simulations, we designed a pair of cuboid-shaped DNA origami structures, Cuboid X and Y. Figures 7c and S15 show the structures in detail. Importantly, we were able to control the orientation of the cuboids on top of the nanocapillary with the help of a guiding leash attached to the different faces of the cuboids. As in the case of the DNA origami plates, we detected the placement of Cuboid X or Y on the nanocapillary tip as a drop in the ionic current until reversal of the voltage polarity ejected the cuboid structure. Figure S15 shows typical

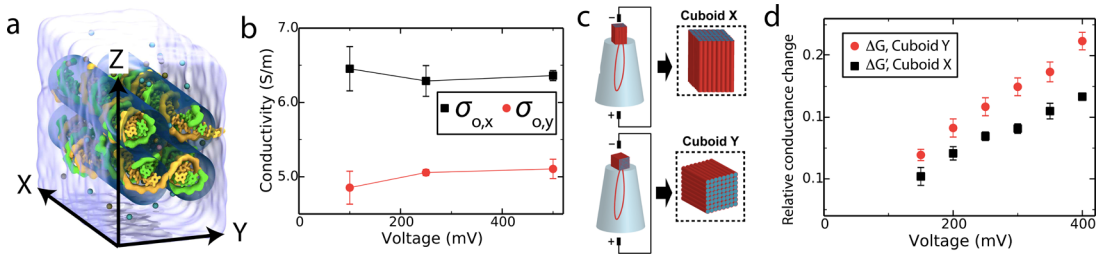

Figure 7. Anisotropic conductivity of DNA origami. (a) Illustration of the m13 SQ2 simulation system solvated in 1 M KCl and 50 mM $MgCl_2$. The scaffold strand (green) and the staples (yellow) are shown. The four semitransparent blue cylinders indicate the locations of the four DNA double helices. By applying electric field in the *x* or *y* direction and measuring the resulting ionic currents, the ionic conductivity of the plate in the *x* and *y* directions, $\sigma_{o,x}$ and $\sigma_{o,y}$, can be computed using a circuit model, Figure S1b,c. (b) Simulated ionic conductivity of the SQ2 plate parallel ($\sigma_{o,x}$) and perpendicular ($\sigma_{o,y}$) to the DNA axis *versus* applied voltage. (c) Schematic of experimental measurements of the anisotropic conductivity of DNA cuboids. DNA origami cuboids are trapped on a nanocapillary in different orientations with the assistance of guiding leashes attached to different sides of the cuboids. Subject to a voltage bias, ionic current passed through Cuboid X along the DNA helices and through Cuboid Y perpendicular to the helices. (d) Relative conductance change for Cuboid X and Cuboid Y systems *versus* applied voltage. The error bars indicate the standard error of mean computed over five independent measurements. The relative conductance change for the Cuboid X system was corrected as described in the text and Supporting Information Methods.

ionic current traces. We repeated trapping and ejection experiments hundreds of times for the same nanocapillary. All experiments were carried out at 1 M KCl, 5 mM $MgCl_2$, 0.5 × TBE (Tris/Borate/EDTA, Table S6) and pH 8.3.

For quantitative analysis, we chose ionic current recordings for each cuboid from five nanocapillaries whose resistances ranged between 50 and 140 MΩ. Representative histograms of the relative conductance change ΔG at different voltages are shown in Figures S17, S18. For nanocapillaries of similar resistances, ΔG appears to be larger for Cuboid Y than for Cuboid X.

To directly compare the relative conductance blockades produced by Cuboids X and Y, we need to account for the fact that the cuboids were longer (29 nm) in one dimension (along DNA helices) than in the other two (both 23 nm). It was previously shown that the conductance of a DNA origami plate is determined mainly by the current that flows through the area directly above the nanopore, transverse to the plate.[46] Thus, we can correct our data by assuming that the resistance of a DNA origami cuboid is simply proportional to its length. Scaling the resistance of Cuboid X by 23/29, we can arrive with an expression for the corrected relative conductance change of cuboid X, $\Delta G_x'$, which can be directly compared to the relative conductance change of Cuboid Y, ΔG_y. The detailed derivation of the correction is given in Supporting Information Methods. Figure 7d compares the relative conductance change of Cuboid Y, ΔG_y to the relative conductance change of Cuboid X, $\Delta G_x'$ corrected for the difference in the dimensions of the cuboids. At all voltages, $\Delta G_x'$ is considerably smaller than ΔG_y. Thus, our measurements indicate that the DNA origami structure is considerably more conductive along the DNA helix direction (Cuboid X) than normal to the DNA helices (Cuboid Y), in agreement with the predictions of the MD simulations.

CONCLUSIONS

Through a combination of computer simulations and experiments we have elucidated determinants and the microscopic mechanism of ion conductivity of DNA origami. It has already been known that the lattice type can affect the ionic conductance of a DNA origami plate.[53] In accordance with the previous studies, our simulations determined the conductance of a square-lattice plate to be approximately twice that of a honeycomb one. Rather unexpectedly, we also found that both the bulk concentration of magnesium ions and the CG content of the DNA origami plate could affect the conductivity of DNA origami *via* the same mechanism, altering the average distance between the DNA helices in the plate. Increasing the concentration of Mg^{2+} makes the plates more compact, reducing their ability to conduct ions. Our results suggest that the leakage current through the DNA origami plates can be reduced by at least half along with the fluctuations of the current, which is expected to increase the sensitivity of ionic current measurements performed using DNA origami-based nanopore sensors.

We found that the structure of DNA origami plates could change in response to the applied electric field. Subject to the same electric field, the two-layer square-lattice plate is considerably more leaky to ions than the four- or six-layer plates because of the greater deformability of the former. Furthermore, we found that switching on and off the electric field can produce reversible changes in the plate structure on a very short (~50 ns) time scale. Our simulations identified the electro-osmotic flow as the microscopic force driving the deformation of the plates. When placed on a solid-state support, the DNA origami both buckles and swells as a result of the competition between the force of the applied field driving the origami into the nanopore and the drag of the electro-osmotic flow swelling the structure. The reversible deformation of DNA origami

structures in electric field may find uses in the design of nanoscale electromechanical switches.

We have also shown that the electrical conductivity of a DNA origami object can be anisotropic. Although materials science knows many examples of inorganic substances that exhibit anisotropic electrical conductivity (for example, graphite), the ability of programming the electric properties of DNA-based nanostructures has not been demonstrated, to the best of our knowledge, until now. The possibility of controlling the direction and magnitude of ionic current within a self-assembled DNA nanostructure is poised to find applications in nanofluidic electronics. Our work demonstrates the predictive power of the MD method in the characterization of synthetic DNA nanostructures.

MATERIALS AND METHODS

Simulations. *General MD Methods.* All molecular dynamics simulations were performed using the program NAMD2,[61] periodic boundary conditions, the CHARMM36 parameter set for water, ions and nucleic acids,[62] CHARMM-compatible parameters for amorphous silicon dioxide,[63] and custom parametrization of ion−DNA and ion−ion interactions.[56] All simulations employed a 2−2−6 fs multiple timestepping, SETTLE algorithm to keep water molecules rigid,[64] RATTLE algorithm to keep all other covalent bonds involving hydrogen atoms rigid,[65] a 8−10−12 Å cutoff for van der Waals and short-range electrostatic forces. Long-range electrostatic interactions were computed using the particle mesh Ewald (PME) method[66] over a 1.2 Å resolution grid.[67]

All-Atom Models of DNA Origami Systems. Using the caDNAno program,[26] we designed 22-by-2 (2 layers), 8-by-4 (4 layers), 4-by-6 (6 layers) square (SQ) lattice DNA origami plates and a honeycomb (HC) lattice plate containing 14 helices arranged as 3 planar hexagons. With the exception of the AT and GC SQ2 systems, for which we provided custom $(AT)_n$ and $(GC)_n$ sequences, the plates were assigned the nucleotide sequence based on the m13mp18 genome by caDNAno. Using the connectivity (.json) and the staple sequence (.csv) files, the caDNAno designs were converted to all-atom structures by the cadnano2pdb program.[55] From the all-atom structures, we extracted 4 (SQ2 and HC2), 8 (SQ4), or 12 (SQ6) helices, forming the minimal repeat units of the corresponding ideal lattice DNA origami designs. Under the periodic boundary conditions, the unit cells formed effectively infinite plates. Figures S3−S5 provide detailed schematics of the designs used for MD simulations. Table S2 lists the nucleotide sequences of the staple strands used to build the all-atom models. The hexagonal structure (HX2*) was made by inserting a 21-bp double helix into the central pore of the HC2 structure. The additional helix was made effectively infinite under periodic boundary conditions. The AT content of the HC2, HX2*, SQ4, SQ6 plates was about 46, 48, 50 and 55%, respectively. Variation of a few percent in the AT content among the plates was expected to have a rather minor effect on the variation of the ionic current among the different designs. The SQ2 hybrid origami structure was 64-bp long and contained two unit cells of SQ2. The sequence and the detailed schematics of the SQ2 hybrid structure can be found in Table S2 and Figure S6, respectively. After the all-atom model of the DNA origami structure was complete, Mg^{2+}-hexahydrates[56] were randomly placed near the structures; water and ions were added using the Solvate and Autoionize plugins of VMD. In x and y, the dimensions of the solvation box were the same as those of the DNA origami. The initial z dimension of the solvation box was about 2−3 times the z dimension of the DNA origami; the z dimension of the system was reduced considerably during the equilibration as water entered the DNA origami structure.

Equilibration of the All-Atom Models. Upon assembly, the systems were minimized using the conjugate gradient method for 9600 steps to remove steric clashes. During the minimization process, every atom of the DNA origami structure was harmonically restrained (with the spring constant k_{spring} = 1 kcal/(mol Å^2)) to its initial coordinates to prevent the structure from breaking. After minimization, the systems were equilibrated under the NPT condition, where the number of atoms (N), pressure (P) and temperature (T) were kept constant. The pressure was set to 1 atm using the Nosé−Hoover Langevin piston method.[68,69] The temperature was maintained at 295 K using a Langevin thermostat.[70] Fluctuations of the system's dimensions along the x, y and z axes were decoupled from one another. The systems were initially equilibrated for ∼2 ns applying harmonic restraints (k_{spring} = 1 kcal/(mol Å^2)) to every atom of the DNA origami. Next, the equilibration was continued for 10 ns applying the same-strength harmonic restraints to the atoms of the DNA bases only (excluding hydrogen atoms), allowing the DNA backbone to relax. Following that, spatial restraints were replaced by a set of harmonic potentials (k_{spring} = 1 kcal/(mol Å^2)) that confined the distances between certain atom pairs in the DNA origami (excluding hydrogen atoms, phosphate groups, atoms in the same nucleotide and pairs separated by more than 10 Å) to their initial values; each system was simulated under such restraints for ∼30 ns. Following that, the DNA origami was equilibrated without any restraints. During all stages of the equilibration process, the integrity of each Mg^{2+}-hexahydrate complex was maintained using harmonic potentials (k_{spring} = 5000 kcal/(mol Å^2)) that kept the distance between the six water molecules and the magnesium ion at 1.94 Å.

Adjustment of Bulk Ion Concentration. To determine and adjust the bulk ion concentration, a system was first simulated under the NPT conditions and no restraints for 48 ns. The resulting MD trajectory was aligned to have the center of mass of the DNA origami at the origin of the system and the solution symmetrically partitioned along the z axis with respect to the DNA origami. The local ion concentration was computed in 1 Å bins along the z axis (normal to the membrane) by averaging over the x−y plane of the MD trajectory. The 5 Å top and bottom layers (10 Å width in total) were used to measure the bulk concentration. The difference between the actual and target bulk concentrations was used to determine the number and type of ions that needed to be added to or removed from the system. Upon adjustment of the number of ions, the systems were minimized for 9600 steps and equilibrated for another 48 ns. The bulk concentration was recalculated and another adjustment to the number of ions was made, if necessary. Obtaining the target concentration within ±20 mM accuracy typically required 2−5 iterations.

Construction of the Hybrid System. The amorphous SiO_2 structure was obtained using a previously described annealing procedure.[63] The final structure measured 12 nm in the x direction, 5.15 nm in y and 8 nm in z. Under periodic boundary conditions, the SiO_2 structure represented an infinite (in the y direction) gap, with the walls of the gap separated by ∼15 nm in the x direction. To construct a hybrid structure, the SQ2-long plate (defined in Figure S6) was placed across the gap 1 nm above the SiO_2 structure. Under the periodic boundary conditions, the DNA origami plate was periodic only in the y direction; the distance between the ends of the origami in the x direction was about ∼5.5 nm. Mg^{2+}-hexahydrate, water, K^+ and Cl^- were added as described above. As the dimension of the hybrid system was fixed in the x and y dimensions, ∼20 ns constant area NPT equilibration was sufficient for the system to attain its equilibrium volume. In all simulations of the hybrid system, each atom of SiO_2 was harmonically restrained to its coordinates obtained at the end of the annealing procedure (with the spring

constant of 20 kcal/(mol Å^2)). A DNA-specific grid-based potential was applied to reduce adhesion of DNA to SiO_2.[71,72]

MD Simulation of Ionic Current. All simulations of the ionic current were performed in the constant number of atom, volume and temperature ensemble. A voltage drop (V) across the system was produced by applying an external electric field E such that $V = -EL$, where L was the length of the simulation system in the direction of the applied field.[58] To determine the dimensions of the system for the constant volume simulations, we first obtained the average $x-y$ cross section area of the system of interest using the last 400 ns of the NPT equilibration. Among the total number of frames of the equilibration trajectory, we chose the one having its $x-y$ cross section area closest to the 400 ns average and started our ionic current simulation using the coordinates of that frame. To prevent the DNA origami from drifting in the electric field, we applied a harmonic constraint to its center of mass using the spring constant of 1 kcal/(mol Å^2). As the $x-y$ cross section area of the SQ2/SiO_2 hybrid system was fixed during the equilibration, the ionic current simulations were performed starting from the last frame of the NPT equilibration; no restraints were applied to the DNA origami plate.

Experiments. *Assembly of Hybrid DNA Origami Nanopores.* For our experiments, we used a DNA origami design consisting of a flat square-shaped plate (57.8 nm (170 bp) × 52.8 nm (24 helices)) that was two helices thick with a ~330 nm long leash of double-stranded DNA facilitating the correct and stable insertion of DNA origami into the nanocapillary.[52] The sequence of base pairs for the single-stranded scaffold and staples was determined by the DNA origami software caDNAno and is given in the Table S3.[26] The 8634 nt-long mutant of the m13mp18-scaffold and 243 staples were mixed in a 1:10 stoichiometric ratio in 16 mM $MgCl_2$, 1 × TE solution, Table S6. In a thermal-annealing cycling process (23 h), the single-stranded DNA fragments self-assembled into tightly interlinked double-helical DNA domains in a square packing lattice. After purification by centrifugation with 100 kDa molecular weight cutoff filters (100 kDa Amicon Ultra, Millipore), the successful assembly of DNA origami plates and the absence of aggregates were confirmed by means of agarose gel electrophoresis and atomic force microscopy (AFM) (see Figure S10).

Design of DNA Origami Cuboids. A pair of cuboid-shaped structures was designed to have the same main body composed of 64 (8 by 8) helices arranged in a square lattice pattern. The length of each helix was 85 base pairs. Thus, the cuboids measured 29 nm along the DNA axis and 23 × 23 nm^2 in cross section, Figure S15. The two cuboid structures differed by the attachment of the guiding leash: the leash of Cuboid X was attached at the end of a DNA helix, whereas the leash of Cuboid Y extended from the middle of a helix; both leashes protruded approximately from the centers of the respective cuboid faces. The leashes had exactly the same length (1777 base pairs) extending up to ~300 nm away from the main body. Folding of each origami cuboid was directed by 138 staples; 45 complementary staples were used to make the leash double stranded. Detailed 2-D design layouts and staple sequences can be found in Figures S19, S20 and Tables S4 and S5. The staples were mixed with 7249 nt-long single-stranded scaffold (m13mp18, purchased from New England Biolabs, Cat N4040S) at a concentration of 100 and 10 nM, respectively. Successful folding was carried out within TE buffer (10 mM Tris-HCl, 1 mM EDTA, pH = 8) with 14 mM $MgCl_2$. Excess staples were left after folding and had to be removed. Centrifugation with molecular weight cutoff filter (100 kDa Amicon Ultra, Millipore) was used for the purification. Electrophoresis and AFM measurements were used for origami characterization. The dominant bands in lane 3 and 4 of the gel image, Figure S15a, correspond to the correctly folded origami structures. The main body and the leash can be clearly seen in the AFM images of the folded structures, Figure S15b,c.

Electrical Recording Using Nanocapillaries. Quartz nanocapillaries with outer diameters of 41 ± 5 nm were fabricated using a laser-assisted pipet puller (Sutter P-2000) and embedded into a polydimethylsiloxane (PDMS) (Sylgard 184, DowCorning) cell with two fluid reservoirs and a connecting channel, as previously described.[52] For nanocapillaries used in DNA origami cuboid measurement, nanocapillaries with the inner diameter of 9.1 ± 2.0 nm were produced by a laser-assisted pipet puller and then imaged with FEI Magellan XHR SEM at 1−2 kV acceleration voltage. An example SEM image of the nanocapillaries and the diameter distribution of 13 nanocapillaries are shown in Figure S16. Two silver wires (diameter 0.2 mm, Advent) were chlorinated (Ag/AgCl) and used as electrodes that were inserted into the two reservoirs containing an electrolyte solution (1 M KCl, varying $MgCl_2$ concentration, buffered with 0.5× TBE, pH ≈ 8.3). Ionic current traces were measured by means of an Axopatch 200B amplifier (Axon Instruments, USA) at a sampling frequency of 100 kHz and with an internal Bessel filter at 10 kHz. The signals were digitized by a NI-PCIe-6251 card (National Instruments, USA) and processed with custom-made LabVIEW routines (LabVIEW 8.6, National Instruments).

Measurements of DNA Origami Conductivity. The DNA origami solution, typically at 0.5 nM in the respective measurement buffer, was added to the reservoir in front of the nanocapillary. As DNA is negatively charged, the DNA origami plates were driven toward the nanocapillary upon applying a positive voltage. We can typically trap the DNA origami structures stably within a voltage range of 300−500 mV. At lower voltages, the structures are not stably trapped, while they translocate at higher voltages as previously reported due to mechanical failure.[52,53] We clearly observe the trapping of a DNA origami plate onto the nanocapillary by the voltage-dependent drop in the ionic current, as shown in Figure 3a. As a result of nonspecific interactions between DNA origami and the quartz surface in the presence of magnesium, reversing the voltage did often not lead to successful ejection of DNA origami from the nanocapillary above 5.5 mM $MgCl_2$. However, by applying a very high positive voltage, *i.e.*, 1000 mV, it was possible to suck the DNA origami through the nanocapillary and recover the original current baseline. Because of the reversibility of the DNA origami insertion process, trappings could be routinely performed up to a few hundred times per voltage step and nanocapillary.[48,52]

Assembly of Fluorescently Labeled DNA Origami Plates. The fluorescently labeled staples were purchased from Integrated DNA Technologies (IDT). The assembly, purification and characterization of the FRET-modified DNA origami plates followed the procedure outlined for the unmodified DNA origami plates with leash as described above. However, light exposure had to be minimized in the assembly and purification processes to avoid fluorophore bleaching. The fluorescently labeled staples are marked in Table S3 in the Supporting Information.

Spectrofluorometry for Emission Measurements. FRET measurements were performed in bulk using a Cary Eclipse Fluorescence Spectrophotometer (Agilent Technologies). It utilized a Xenon flash lamp to excite the sample at a single constant wavelength. An emission intensity spectrum was then collected over a range of wavelengths in an orientation of 90° to the exciting light. In our experiments, the excitation wavelength was set to 521 nm and the wavelength range 550−700 nm was scanned to obtain the emission spectra. The excitation slit was set to 20 nm. The FRET-modified DNA origami sample was diluted to a final concentration of ~2 nM in a low volume cuvette (70 μL) (Sigma-Aldrich). Emission spectra were taken in various solutions buffered with 0.5× TBE, $MgCl_2$ concentrations ranging from 5.5 to 205.5 mM and at a background concentration of 1 M KCl. $MgCl_2$ was added to the same cuvette gradually and the evolution of emission spectra was observed.

Conflict of Interest: The authors declare no competing financial interest.

Acknowledgment. C.Y.L., J.Y. and A.A. were supported in part by the grants from the National Science Foundation (DMR-0955959, PHY-1430124 and ECC-1227034), and the National Institutes of Health (R01-HG007406). E.A.H. acknowledges support from Schweizerische Studienstiftung (Swiss Study Foundation) and Gonville & Caius College. S.H.A. acknowledges support from a Herchel Smith postdoctoral fellowship. J.K. acknowledges support from Chinese Scholarship Council and

Cambridge Overseas Trust. U.F.K. was supported by an ERC starting grant (PassMembrane, 261101). The authors gladly acknowledge supercomputer time provided through XSEDE Allocation Grant MCA05S028 and the Blue Waters Sustained Petascale Computer System (UIUC).

Supporting Information Available: Detailed description of DNA origami designs, methods used to compute the ionic current, 3D flux and ionic conductivity, selected properties of the simulated systems, experimental gel and FRET assays, animations illustrating selected MD trajectories. This material is available free of charge *via* the Internet at http://pubs.acs.org.

REFERENCES AND NOTES

1. Dekker, C. Solid-State Nanopores. *Nat. Nanotechnol.* **2007**, *2*, 209–215.
2. Kasianowicz, J.; Robertson, J. W. F.; Chan, E. R.; Reiner, J. E.; Stanford, V. M. Nanoscopic Porous Sensors. *Annu. Rev. Anal. Chem.* **2008**, *1*, 737–766.
3. Howorka, S.; Siwy, Z. Nanopore Analytics: Sensing of Single Molecules. *Chem. Soc. Rev.* **2009**, *38*, 2360–2384.
4. Wanunu, M. Nanopores: A Journey Towards DNA Sequencing. *Phys. Life Rev.* **2012**, *9*, 125–158.
5. Kasianowicz, J. J.; Brandin, E.; Branton, D.; Deamer, D. W. Characterization of Individual Polynucleotide Molecules Using a Membrane Channel. *Proc. Natl. Acad. Sci. U. S. A.* **1996**, *93*, 13770–13773.
6. Li, J.; Stein, D.; McMullan, C.; Branton, D.; Aziz, M. J.; Golovchenko, J. A. Ion-beam Sculpting at Nanometre Length Scales. *Nature* **2001**, *412*, 166–169.
7. Vercoutere, W. A.; Winters-Hilt, S.; DeGuzman, V. S.; Deamer, D.; Ridino, S. E.; Rodgers, J. T.; Olsen, H. E.; Marziali, A.; Akeson, M. Discrimination among Individual Watson-Crick Base Pairs at the Termini of Single DNA Hairpin Molecules. *Nucleic Acids Res.* **2003**, *31*, 1311–1318.
8. Clarke, J.; Wu, H.; Jayasinghe, L.; Patel, A.; Reid, S.; Bayley, H. Continuous Base Identification for Single-Molecule Nanopore DNA Sequencing. *Nat. Nanotechnol.* **2009**, *4*, 265–270.
9. Reiner, J. E.; Balijepalli, A.; Robertson, J. W. F.; Drown, B. S.; Burden, D. L.; Kasianowicz, J. J. The Effects of Diffusion on an Exonuclease/Nanopore-Based DNA Sequencing Engine. *J. Chem. Phys.* **2012**, *137*, 214903.
10. Kumar, S.; Tao, C.; Chien, M.; Hellner, B.; Balijepalli, A.; Robertson, J. W. F.; Li, Z.; Russo, J. J.; Reiner, J. E.; Kasianowicz, J. J.; *et al.* PEG-Labeled Nucleotides and Nanopore Detection for Single Molecule DNA Sequencing by Synthesis. *Sci. Rep.* **2012**, *2*, 684.
11. Skinner, G. M.; van den Hout, M.; Broekmans, O.; Dekker, C.; Dekker, N. H. Distinguishing Single- and Double-Stranded Nucleic Acid Molecules Using Solid-State Nanopores. *Nano Lett.* **2009**, *9*, 2953–2960.
12. Wanunu, M.; Bhattacharya, S.; Xie, Y.; Tor, Y.; Aksimentiev, A.; Drndic, M. Nanopore Analysis of Individual RNA/Antibiotic Complexes. *ACS Nano* **2011**, *5*, 9345–9353.
13. Manrao, E.; Derrington, I.; Pavlenok, M.; Niederweis, M.; Gundlach, J. Nucleotide Discrimination with DNA Immobilized in the MspA Nanopore. *PLoS One* **2011**, *6*, 25723.
14. Venta, K.; Shemer, G.; Puster, M.; Rodriguez-Manzo, J. A.; Balan, A.; Rosenstein, J. K.; Shepard, K.; Drndic, M. Differentiation of Short, Single-Stranded DNA Homopolymers in Solid-State Nanopores. *ACS Nano* **2013**, *7*, 4629–4636.
15. Keyser, U. F. Controlling Molecular Transport through Nanopores. *J. R. Soc., Interface* **2011**, *8*, 1369–1378.
16. Wei, R.; Gatterdam, V.; Wieneke, R.; Tampe, R.; Rant, U. Stochastic Sensing of Proteins with Receptor-Modified Solid-State Nanopores. *Nat. Nanotechnol.* **2012**, *7*, 257–263.
17. Yusko, E.; Prangkio, P.; Sept, D.; Rollings, R.; Li, J.; Mayer, M. Single Particle Characterization of Aβ Oligomers in Solution. *ACS Nano* **2012**, *6*, 5909–5919.
18. L. Movileanu, J. S.; Schmittschmitt, J. P.; Bayley, H. Interactions of Peptides with a Protein Pore. *Biophys. J.* **2005**, *89*, 1030–1045.
19. Wanunu, M.; Meller, A. Chemically Modified Solid-State Nanopores. *Nano Lett.* **2007**, *7*, 1580–1585.
20. Hou, X.; Guo, W.; Jiang, L. Biomimetic Smart Nanopores and Nanochannels. *Chem. Soc. Rev.* **2011**, *40*, 2385–2401.
21. Hall, A.; Scott, A.; Rotem, D.; Mehta, K.; Bayley, H.; Dekker, C. Hybrid Pore Formation by Directed Insertion of α-Haemolysin into Solid-State Nanopores. *Nat. Nanotechnol.* **2010**, *5*, 874–877.
22. Yusko, E.; Johnson, J.; Majd, S.; Prangkio, P.; Rollings, R.; Li, J.; Yang, J.; Mayer, M. Controlling Protein Translocation through Nanopores with Bio-Inspired Fluid Walls. *Nat. Nanotechnol.* **2011**, *6*, 253–260.
23. Venkatesan, B. M.; Polans, J.; Comer, J.; Sridhar, S.; Wendell, D.; Aksimentiev, A.; Bashir, R. Lipid Bilayer Coated Al_2O_3 Nanopore Sensors: Towards a Hybrid Biological Solid-State Nanopore. *Biomed. Microdevices* **2011**, *13*, 671–682.
24. Hernández-Ainsa, S.; Muus, C.; Bell, N. A. W.; Steinbock, L. J.; Thacker, V. V.; Keyser, U. F. Lipid-Coated Nanocapillaries for DNA Sensing. *Analyst (Cambridge, U. K.)* **2013**, *138*, 104–106.
25. Rothemund, P. Folding DNA to Create Nanoscale Shapes and Patterns. *Nature* **2006**, *440*, 297–302.
26. Douglas, S. M.; Dietz, H.; Liedl, T.; Högberg, B.; Graf, F.; Shih, W. M. Self-Assembly of DNA into Nanoscale Three-Dimensional Shapes. *Nature* **2009**, *459*, 414–418.
27. Ke, Y.; Douglas, S. M.; Liu, M.; Sharma, J.; Cheng, A.; Leung, A.; Liu, Y.; Shih, W. M.; Yan, H. Multilayer DNA Origami Packed on a Square Lattice. *J. Am. Chem. Soc.* **2009**, *131*, 15903–15908.
28. Seeman, N. C. Nanomaterials Based on DNA. *Annu. Rev. Biochem.* **2010**, *79*, 65–87.
29. Pinheiro, A. V.; Han, D.; Shih, W. M.; Yan, H. Challenges and Opportunities for Structural DNA Nanotechnology. *Nat. Nanotechnol.* **2011**, *6*, 763–772.
30. Tørring, T.; Voigt, N. V.; Nangreave, J.; Yan, H.; Gothelf, K. V. DNA Origami: A Quantum Leap for Self-Assembly of Complex Structures. *Chem. Soc. Rev.* **2011**, *40*, 5636–5646.
31. Ke, Y.; Voigt, N. V.; Gothelf, K. V.; Shih, W. M. Multilayer DNA Origami Packed on Hexagonal and Hybrid Lattices. *J. Am. Chem. Soc.* **2012**, *134*, 1770–1774.
32. Andersen, E. S.; Dong, M.; Nielsen, M. M.; Jahn, K.; Subramani, R.; Mamdouh, W.; Golas, M. M.; Sander, B.; Stark, H.; Oliveira, C. L. P.; *et al.* Self-Assembly of a Nanoscale DNA Box with a Controllable Lid. *Nature* **2009**, *459*, 73–76.
33. Voigt, N. V.; Tørring, T.; Rotaru, A.; Jacobsen, M. F.; Ravnsbæk, J. B.; Subramani, R.; Mamdouh, W.; Kjems, J.; Mokhir, A.; Besenbacher, F.; *et al.* Single-Molecule Chemical Reactions on DNA Origami. *Nat. Nanotechnol.* **2010**, *5*, 200–203.
34. Acuna, G. P.; Möller, F. M.; Holzmeister, P.; Beater, S.; Lalkens, B.; Tinnefeld, P. Fluorescence Enhancement at Docking Sites of DNA-Directed Self-Assembled Nanoantennas. *Science* **2012**, *338*, 506–510.
35. Fu, J.; Liu, M.; Liu, Y.; Woodbury, N. W.; Yan, H. Interenzyme Substrate Diffusion for an Enzyme Cascade Organized on Spatially Addressable DNA Nanostructures. *J. Am. Chem. Soc.* **2012**, *134*, 5516–5519.
36. Kuzyk, A.; Schreiber, R.; Fan, Z.; Pardatscher, G.; Roller, E.-M. M.; Högele, A.; Simmel, F. C.; Govorov, A. O.; Liedl, T. DNA-Based Self-Assembly of Chiral Plasmonic Nanostructures with Tailored Optical Response. *Nature* **2012**, *483*, 311–314.
37. Tintoré, M.; Gállego, I.; Manning, B.; Eritja, R.; Fàbrega, C. DNA Origami as a DNA Repair Nanosensor at the Single-Molecule Level. *Angew. Chem., Int. Ed.* **2013**, *52*, 7747–7750.
38. Endo, M.; Sugiyama, H. Single-Molecule Imaging of Dynamic Motions of Biomolecules in DNA Origami Nanostructures Using High-Speed Atomic Force Microscopy. *Acc. Chem. Res.* **2014**, *47*, 1645–1653.
39. Wang, Z.-G.; Ding, B. Engineering DNA Self-Assemblies as Templates for Functional Nanostructures. *Acc. Chem. Res.* **2014**, *47*, 1654–1662.
40. Tsukanov, R.; Tomov, T. E.; Liber, M.; Berger, Y.; Nir, E. Developing DNA Nanotechnology Using Single-Molecule Fluorescence. *Acc. Chem. Res.* **2014**, *47*, 1789–1798.

41. Thacker, V. V.; Herrmann, L. O.; Sigle, D. O.; Zhang, T.; Liedl, T.; Baumberg, J. J.; Keyser, U. F. DNA Origami Based Assembly of Gold Nanoparticle Dimers for Surface-Enhanced Raman Scattering. *Nat. Commun.* **2014**, *5*, 3448.
42. Hernández-Ainsa, S.; Keyser, U. F. DNA Origami Nanopores: An Emerging Tool in Biomedicine. *Nanomedicine (London, U. K.)* **2013**, *8*, 1551–1554.
43. Bell, N. A. W.; Keyser, U. F. Nanopores Formed by DNA Origami: A Review. *FEBS Lett.* **2014**, *588*, 3564–3570.
44. Hernández-Ainsa, S.; Keyser, U. F. DNA Origami Nanopores: Developments, Challenges and Perspectives. *Nanoscale* **2014**, *6*, 14121–14132.
45. Bell, N. A. W.; Engst, C. R.; Ablay, M.; Divitini, G.; Ducati, C.; Liedl, T.; Keyser, U. F. DNA Origami Nanopores. *Nano Lett.* **2012**, *12*, 512–517.
46. Wei, R.; Martin, T. G.; Rant, U.; Dietz, H. DNA Origami Gatekeepers for Solid-State Nanopores. *Angew. Chem., Int. Ed.* **2012**, *51*, 4864–4867.
47. Langecker, M.; Arnaut, V.; Martin, T. G.; List, J.; Renner, S.; Mayer, M.; Dietz, H.; Simmel, F. C. Synthetic Lipid Membrane Channels Formed by Designed DNA Nanostructures. *Science* **2012**, *338*, 932–936.
48. Hernández-Ainsa, S.; Bell, N. A. W.; Thacker, V. V.; Göpfrich, K.; Misiunas, K.; Fuentes-Perez, M. E.; Moreno-Herrero, F.; Keyser, U. F. DNA Origami Nanopores for Controlling DNA Translocation. *ACS Nano* **2013**, *7*, 6024–6030.
49. Burns, J. R.; Stulz, E.; Howorka, S. Self-Assembled DNA Nanopores That Span Lipid Bilayers. *Nano Lett.* **2013**, *13*, 2351–2356.
50. Burns, J. R.; Göpfrich, K.; Wood, J. W.; Thacker, V. V.; Stulz, E.; Keyser, U. F.; Howorka, S. Lipid-Bilayer-Spanning DNA Nanopores with a Bifunctional Porphyrin Anchor. *Angew. Chem., Int. Ed.* **2013**, *52*, 12069–12072.
51. Bell, N. A. W.; Thacker, V. V.; Hernández-Ainsa, S.; Fuentes-Perez, M. E.; Moreno-Herrero, F.; Liedl, T.; Keyser, U. F. Multiplexed Ionic Current Sensing with Glass Nanopores. *Lab Chip* **2013**, *13*, 1859–1862.
52. Hernández-Ainsa, S.; Misiunas, K.; Thacker, V. V.; Hemmig, E. A.; Keyser, U. F. Voltage-Dependent Properties of DNA Origami Nanopores. *Nano Lett.* **2014**, *14*, 1270–1274.
53. Plesa, C.; Ananth, A. N.; Linko, V.; Gülcher, C.; Katan, A. J.; Dietz, H.; Dekker, C. Ionic Permeability and Mechanical Properties of DNA Origami Nanoplates on Solid-State Nanopores. *ACS Nano* **2014**, *8*, 35–43.
54. Douglas, S. M.; Marblestone, A. H.; Teerapittayanon, S.; Vazquez, A.; Church, G. M.; Shih, W. M. Rapid Prototyping of 3D DNA-Origami Shapes with caDNAno. *Nucleic Acids Res.* **2009**, *37*, 5001–5006.
55. Yoo, J.; Aksimentiev, A. *In Situ* Structure and Dynamics of DNA Origami Determined through Molecular Dynamics Simulations. *Proc. Natl. Acad. Sci. U. S. A.* **2013**, *110*, 20099–20104.
56. Yoo, J.; Aksimentiev, A. Improved Parametrization of Li^+, Na^+, K^+, and Mg^{2+} Ions for All-Atom Molecular Dynamics Simulations of Nucleic Acid Systems. *J. Phys. Chem. Lett.* **2012**, *3*, 45–50.
57. Yoo, J.; Aksimentiev, A. Competitive Binding of Cations to Duplex DNA Revealed through Molecular Dynamics Simulations. *J. Phys. Chem. B* **2012**, *116*, 12946–12954.
58. Aksimentiev, A.; Schulten, K. Imaging Alpha-Hemolysin with Molecular Dynamics: Ionic Conductance, Osmotic Permeability and the Electrostatic Potential Map. *Biophys. J.* **2005**, *88*, 3745–3761.
59. Li, W.; Nordenskiöld, L.; Zhou, R.; Mu, Y. Conformation-Dependent DNA Attraction. *Nanoscale* **2014**, *6*, 7085–7092.
60. Luan, B.; Aksimentiev, A. Electro-Osmotic Screening of the DNA Charge in a Nanopore. *Phys. Rev. E: Stat., Nonlinear, Soft Matter Phys.* **2008**, *78*, 021912.
61. Phillips, J. C.; Braun, R.; Wang, W.; Gumbart, J.; Tajkhorshid, E.; Villa, E.; Chipot, C.; Skeel, R. D.; Kale, L.; Schulten, K. Scalable Molecular Dynamics with NAMD. *J. Comput. Chem.* **2005**, *26*, 1781–1802.
62. MacKerell, A. D., Jr.; Bashford, D.; Bellott, M.; Dunbrack, R. L., Jr.; Evanseck, J.; Field, M. J.; Fischer, S.; Gao, J.; Guo, H.; Ha, S.; *et al.* All-Atom Empirical Potential for Molecular Modeling and Dynamics Studies of Proteins. *J. Phys. Chem. B* **1998**, *102*, 3586–3616.
63. Cruz-Chu, E. R.; Aksimentiev, A.; Schulten, K. Water-Silica Force Field for Simulating Nanodevices. *J. Phys. Chem. B* **2006**, *110*, 21497–21508.
64. Miyamoto, S.; Kollman, P. A. SETTLE: An Analytical Version of the SHAKE and RATTLE Algorithm for Rigid Water Molecules. *J. Comput. Chem.* **1992**, *13*, 952–962.
65. Andersen, H. RATTLE: A "Velocity" Version of the SHAKE Algorithm for Molecular Dynamics Calculations. *J. Comput. Phys.* **1983**, *52*, 24–34.
66. Batcho, P. F.; Case, D. A.; Schlick, T. Optimized Particle-Mesh Ewald/Multiple-Time Step Integration for Molecular Dynamics Simulations. *J. Chem. Phys.* **2001**, *115*, 4003–4018.
67. Skeel, R.; Hardy, D.; Phillips, J. Correcting Mesh-Based Force Calculations to Conserve Both Energy and Momentum in Molecular Dynamics Simulations. *J. Comput. Phys.* **2007**, *225*, 1–5.
68. Martyna, G. J.; Tobias, D. J.; Klein, M. L. Constant Pressure Molecular Dynamics Algorithms. *J. Chem. Phys.* **1994**, *101*, 4177–4189.
69. Feller, S. E.; Zhang, Y. H.; Pastor, R. W.; Brooks, B. R. Constant Pressure Molecular Dynamics Simulation—the Langevin Piston Method. *J. Chem. Phys.* **1995**, *103*, 4613–4621.
70. Brünger, A. T. *X-PLOR*, Version 3.1: A System for X-ray Crystallography and NMR. The Howard Hughes Medical Institute and Department of Molecular Biophysics and Biochemistry, Yale University: New Haven, CT, 1992.
71. Wells, D. B.; Abramkina, V.; Aksimentiev, A. Exploring Transmembrane Transport through α-Hemolysin with Grid-Steered Molecular Dynamics. *J. Chem. Phys.* **2007**, *127*, 125101.
72. Belkin, M.; Maffeo, C.; Wells, D. B.; Aksimentiev, A. Stretching and Controlled Motion of Single-Stranded DNA in Locally Heated Solid-State Nanopores. *ACS Nano* **2013**, *7*, 6816–6824.